

Elastic properties of rock salt: Laboratory measurements and Gulf of Mexico well-log analysis

Jingjing Zong¹, Robert R. Stewart¹, Nikolay Dyaur¹, and Michael T. Myers²

ABSTRACT

Rock salt (essentially halite) is a special type of sedimentary rock that has played a large role throughout tectonic and economic history. The unique physical properties of halite (ductility, low density, flowability, and impermeability) can be critical factors in hydrocarbon traps and underground storage. However, seismic imaging and interpretation can be challenging when salt structures are present due to their complex geometry and large impedance contrasts relative to surrounding rocks. To investigate the properties of rock salt in terms of elastic parameters, we use ultrasonic laboratory measurements and well logs. In the laboratory, we have analyzed the effects of composition, crystalline structure, pressure, and temperature on the elastic behavior of a variety of rock salt samples. The samples include pure halite (>95 wt%) from the Gulf of Mexico (GOM) area, argillaceous rock salt from the Zipaquirá Mine, Colombia, and crystalline salt from the

Goderich Mine, Canada. Current measurements suggest that the GOM salt cores behave isotropically in general. The Zipaquirá salt samples show velocity and density variations on account of their heterogeneous composition. The Goderich halite crystals display distinct cubic anisotropy. Measurements on the GOM samples at varying confining pressures and temperatures indicate that increasing pressure elevates velocity whereas increasing temperature decreases velocity. From the analysis of 145 log suites from boreholes drilled through rock salt in the northern GOM, we found that, within the salt formations, P-wave velocities increased slightly with depth (approximately 5 m/s per km). The S-wave velocities from three wells range from 2280 to 2580 m/s. Bulk densities from all the wells cluster at $2160 \pm 30 \text{ kg/m}^3$. These laboratory and log measurements provide new values for the elastic properties of rock salt, which can assist in velocity model building, synthetic seismogram generation, and the understanding of the rock physics of halite.

INTRODUCTION

A widely accepted model for salt diagenesis describes seawater being concurrently evaporated and replenished in a restricted region, which gives rise to salt precipitation into basin-wide beds (Raup, 1970; Gevantman et al., 1981). The depositional environment controls the crystal textures of major evaporites (e.g., halite and gypsum) and the stratigraphy or interlayering during precipitation (Leslie et al., 1997). Salt diapirs and intrusions are likely to be driven later by differential loading and the buoyancy of salt bodies (Hudec and Jackson, 2007).

Considerable attention has focused on pre- and subsalt imaging, with some of the world's largest hydrocarbon discoveries being

located near salt bodies (Jackson et al., 2008). Seismic imaging around salt structures is challenging due to their complex geometry, large velocity contrast relative to their surroundings, and occasional dissolution-collapse features (Leveille et al., 2011). A constant salt velocity is often used in seismic processing, e.g., a V_P of 4480 m/s and V_S of 2590 m/s (Leaney et al., 2004; Willis et al., 2006). Some studies have considered the variabilities inside salt domes, e.g., the dirty salt model (Ji et al., 2011), and the seismic anisotropy of salt due to tectonic stress and the preferred orientation of the halite's lattice (Brown and Sun, 1993; Davison et al., 1996; Raymer et al., 2000a, 2000b).

We have studied a variety of salt samples from three distinct environments: the highly mobilized Gulf of Mexico (GOM) area; the compositionally complicated Zipaquirá Salt Mine, Colombia; and the

Manuscript received by the Editor 9 October 2016; revised manuscript received 27 March 2017; published ahead of production 21 June 2017; published online 11 August 2017.

¹University of Houston, Department of Earth and Atmospheric Sciences, Allied Geophysical Laboratories, Houston, Texas, USA. E-mail: jzong@uh.edu; rrstewart@uh.edu; nidyaury@gmail.com.

²University of Houston, Cullen College of Engineering, Department of Petroleum Engineering, Houston, Texas, USA. E-mail: mtmyers@uh.edu.
© 2017 Society of Exploration Geophysicists. All rights reserved.

Goderich Mine of Sifto Canada Corporation in the stable Michigan Basin (Figure 1). In the GOM, where allochthonous salt structures are plentiful and significant, we selected samples from the Hockley Salt Dome, Texas, and the Bayou Corne Salt Dome, Louisiana.

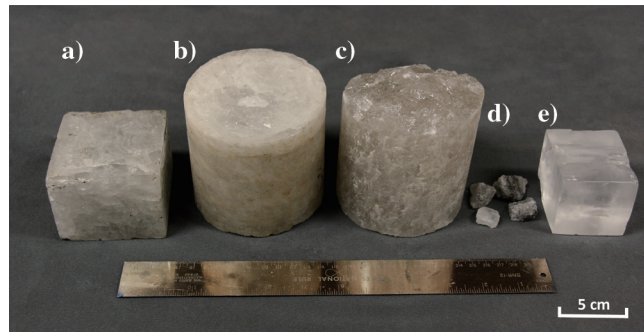


Figure 1. Rock-salt samples. (a) Wall outcrop shaped into a block and (b) salt core from a horizontal well, both from the Hockley Salt Dome. (c) Salt core from the Bayou Corne Salt Dome. (d) Salt samples from the Zipaquirá Salt Mine. (e) Halite crystal sample from the Goderich Mine.

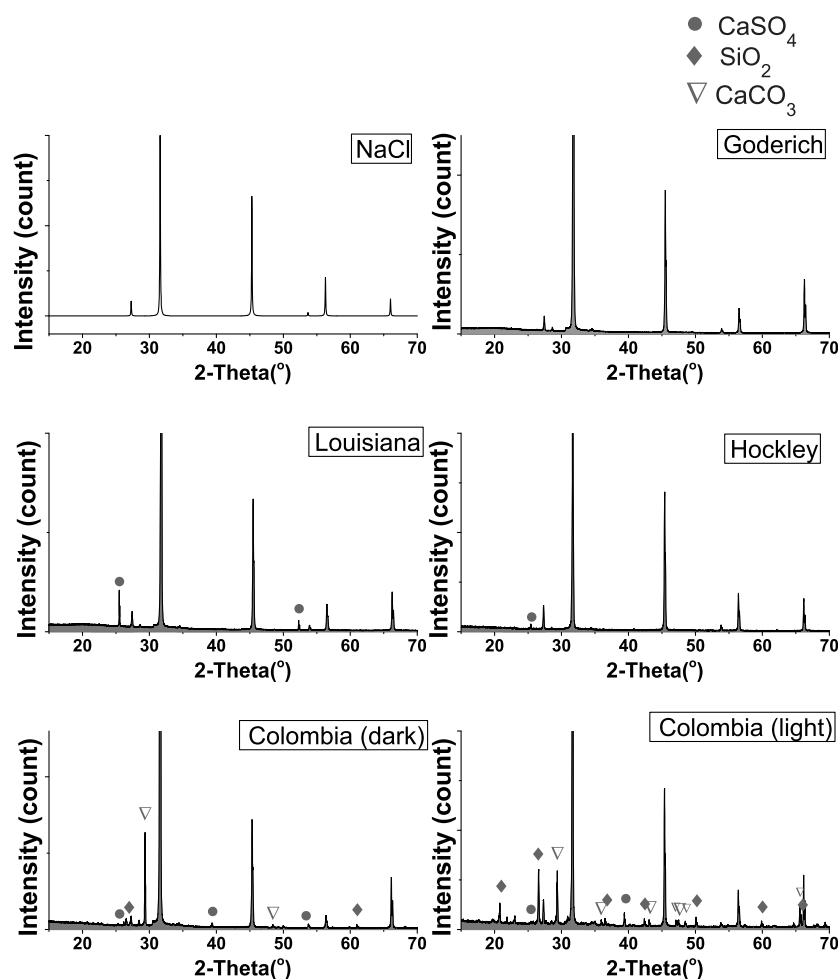


Figure 2. Composition analysis from XRD measurements shows the signatures of different compounds in the salt samples.

Having been deposited with argillaceous halite and embedded with clay layers, the Zipaquirá salt samples were chosen for their heterogeneity. Salt samples from the autochthonous Goderich Mine were of interest because of their well-preserved cubic crystalline structure. We extended our salt study to in situ field conditions using the sonic and density logs from 145 wells drilled through salt in the northern GOM. These well logs provided in situ elastic values of salt to complement our laboratory results. As salt domes are of intense interest in the GOM (and elsewhere), our study provides information for velocity model building as well as for synthetic seismogram generation.

METHODS

Mineralogical analysis

We first conducted an X-ray powder diffraction (XRD) and an inductively coupled plasma-mass spectrometry (ICP-MS) to determine the composition of all samples. Figure 2 shows the XRD analysis results: Halite (NaCl) was the dominant component for all the samples. The ICP-MS results were similar to the XRD findings, but they provided a complementary elemental composition and weight ratio (Table 1). The Goderich crystal samples were nearly pure halite (> 99 wt%). The GOM salt samples were very pure halite (> 97 wt%) with a small amount (< 2 wt%) of anhydrite (CaSO_4). The Zipaquirá salt samples contained considerable amounts of anhydrite, silicate (SiO_4), and calcium carbonate (CaCO_3).

Density measurements

Samples were weighed using a digital analytical balance, in and out of a water container. Density was estimated using the hydrostatic weighing method (Pratten, 1981) and the weight/volume method as follows:

Density of sample

$$= \frac{(\text{Density of water}) * (\text{Weight of sample})}{(\text{Weight of sample}) - (\text{Weight of immersed sample})} \quad (1)$$

We applied waterproof covers to prevent the salt samples from dissolution. Regularly shaped samples were wrapped in aluminum foil, whereas irregularly shaped samples were covered with melted paraffin before submerging. The weight and volume of the applied aluminum, paraffin covers, and the suspension threads were measured and corrected for in the final sample density calculation. The balance has an accuracy of 0.001 g, resulting in an error of approximately 0.04% for the lightest sample. We repeated three measurements for each sample and used the average values. The standard deviations give the range of our measurements.

Ultrasonic velocity measurements

The ultrasonic pulse-transmission method is often used to find the velocity of geologic mate-

rials (Mavko and Nolen-Hoeksema, 1994; Vernik and Liu, 1997; Stewart et al., 2012). In our measurements, we used 0.5 MHz shear transducers and 1 MHz compressional transducers. To make a measurement, one pair of ultrasonic transducers were mounted

on a benchtop system, pressed against either side of the sample while facing each other (see Figure 3). The benchtop system used an Olympus Pulser-Receiver 5077PR for signal control. A digital oscilloscope (Handyscope HS4) was connected to a computer for display and analysis. The oscilloscope had a 50 MHz maximum sampling rate, which gave the picking time limit as 20 ns. The samples had propagation times of 3–40 µs for the P- and S-waves, which led to a picking error of 0.05%–0.67%. The source transducer generates an ultrasonic P- or S-wave, which travels through the sample and is recorded by the receiving transducer. Transducer calibrations were undertaken before measurements to correct for system delays using aluminum blocks of varying lengths. Figure 4 shows an example calibration for the 500 kHz transducers. Velocity was directly calculated from wave travel distance (sample length) and wave traveltimes. For length measurements, we used an electronic caliper with an accuracy of 0.01 mm. It yielded a maximum error of 0.08% for the samples studied (length of 12–80 mm).

X-ray computerized tomography scanning

To better understand the effects of pressure on salt grains, we undertook X-ray computerized tomography (CT) scanning before and after the triaxial pressure tests. CT scanning has been widely used to visualize fractures and structural changes in rock samples; it shows how density and microfractures can change under pressure (Davison et al., 2012).

LABORATORY MEASUREMENTS

Rock-salt samples from the Gulf of Mexico area

We measured the velocity and density for salt samples collected from the Hockley Salt Dome and Bayou Corne Salt Dome. These two salt domes sit in the East Texas-South Louisiana salt-dome basin and were sourced by the Jurassic Louann Salt deposition (Anderson et al., 1973; Jackson, 1984). The rock-salt samples are characterized by coarse halite aggregates with grain sizes from 3 to 30 mm. A series of measurements were designed to obtain the

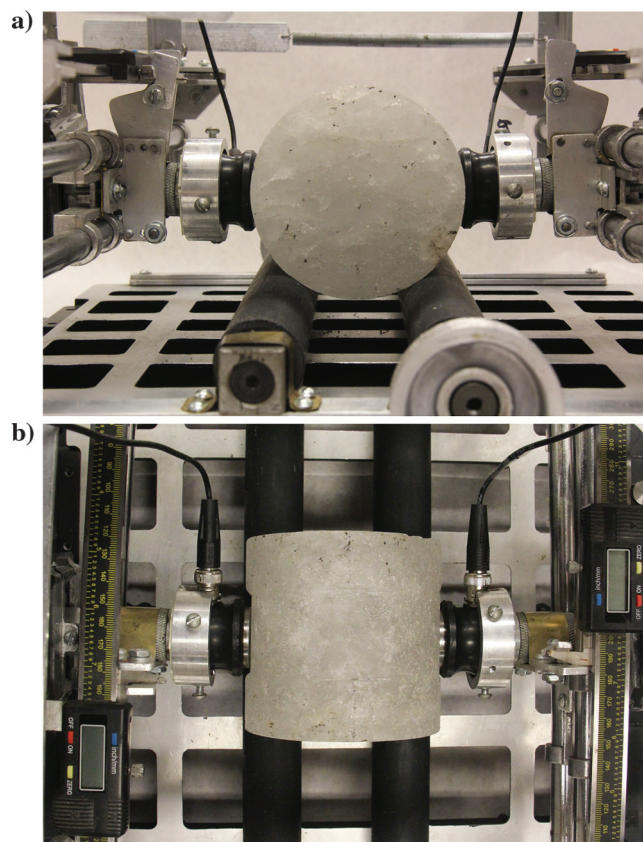


Figure 3. Photographs of the Hockley Salt Dome sample and ultrasonic apparatus. (a) Sample axial view and (b) top view of a sample placed between the source and receiver ultrasonic transducers with couplant.

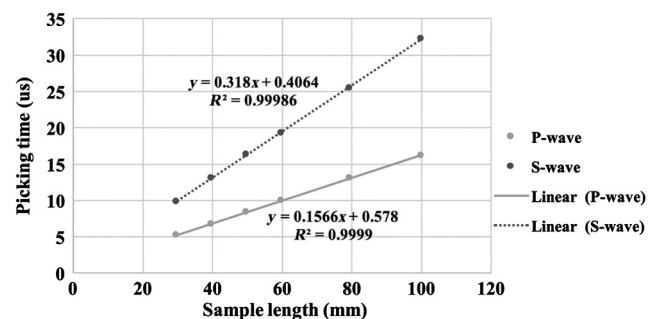


Figure 4. An example of the transducer delay-time calibration. We use aluminum blocks with increasing length from 30 to 100 mm. The slopes of the fitting lines are the slownesses of aluminum for P- and S-waves. The intercepts at the vertical axis are the delay times.

velocities in different propagation directions of the P- and S-waves. For cylindrical salt cores, we transmitted the P- and S-waves across the core as shown in Figure 5a. We rotated the core at 10° intervals to record P- and S-waves in different propagation directions (seen in Figure 5b). For rectangular-shaped samples, we chose three mutually orthogonal axes: X, Y, and Z as the wave-propagation directions. The shear-transducer generates an S-wave polarized perpendicular to its propagation direction. We investigated V_S variations at different polarization angles by rotating the source and receiver transducers simultaneously to keep the S-wave polarized in the plane perpendicular to the S-wave propagation direction. As seen in Figure 5c and 5d, the double-headed arrows represent the S-wave polarization direction, whereas the black arrows indicate the wave-propagation direction. To further understand the thermal and stress effects in the subsurface, we also conducted ultrasonic pulse transmission tests at varying confining pressures and temperatures on the Bayou Corne salt samples.

Measurements at room temperature and pressure

We measured two salt core samples from the Hockley Salt Dome and one salt block excavated from the Hockley Salt Mine, at room conditions of approximately 25°C, 1 atm, and relative humidity of 46%. The Hockley salt samples H_1 and H_2 came from salt cores 101.60 mm (4 in) in diameter from horizontal wells, at a depth of approximately 460 m. The measured samples contained more than 98 wt% halite and approximately 1 wt% anhydrite.

We measured H_1 in its original cylindrical shape. We rotated the sample about its core axis and measured at 10° intervals.

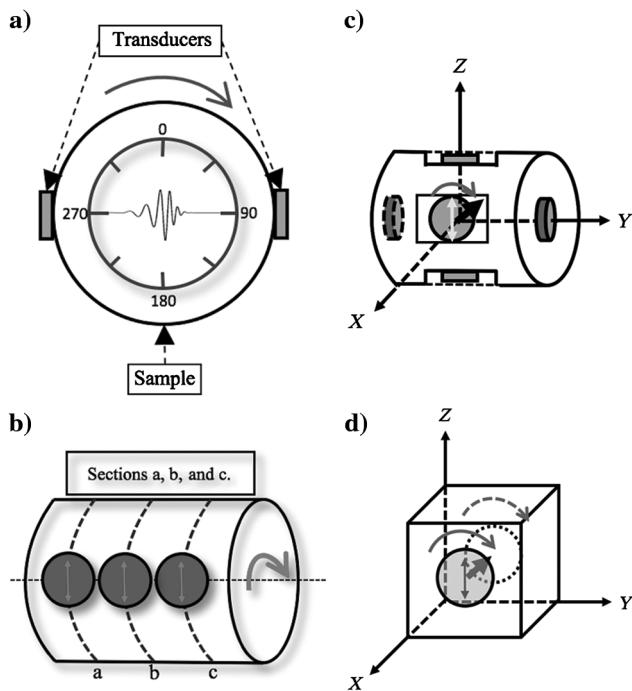


Figure 5. Measurement methods for the Hockley samples. (a) H_1 axial view and (b) side view. The same measurements were taken in three equally spaced sections 30 mm apart. (c and d) Schematic diagrams for the measurements on H_2 and H_3 , respectively. The transducers were rotated synchronously about the three orthogonal axes, whereas H_2 and H_3 were fixed.

The S-wave remained vertically polarized during rotation. We repeated the same measurements in three parallel sections, *a*, *b*, and *c*, as is shown in Figure 5b. As seen in Figure 6a and 6b, V_P and V_S from all propagation directions were approximately isotropic. Small variations may have been caused by previous stress effects, interior microfractures, or cracking during and after drilling. The average V_P and V_S are included in Table 2.

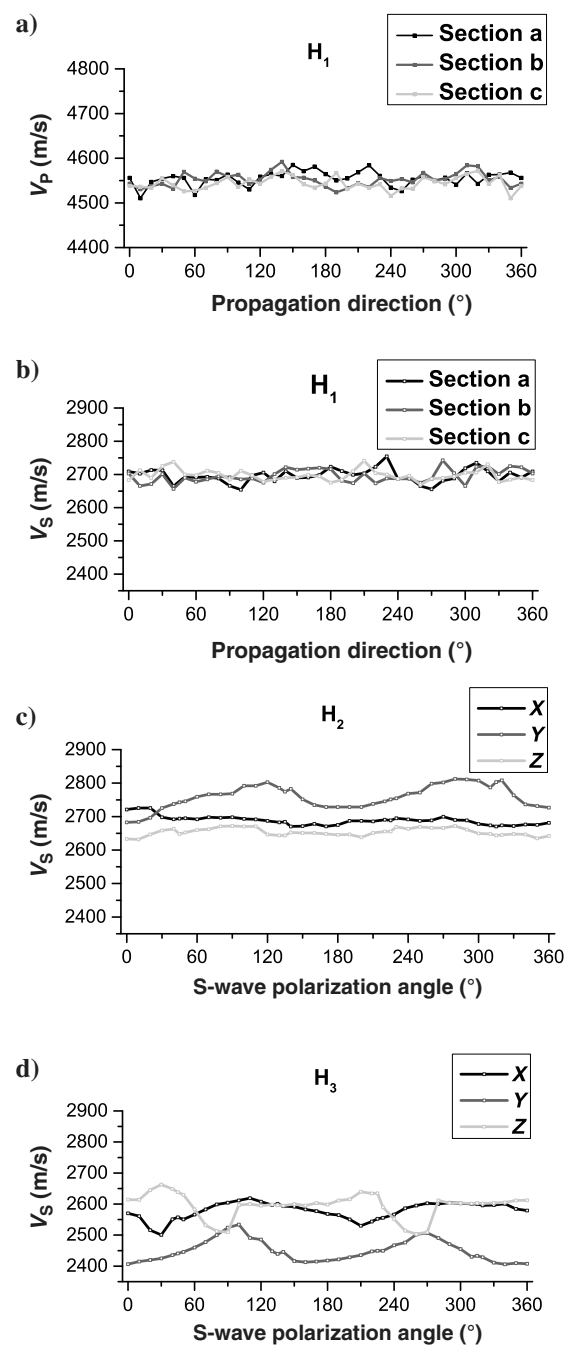


Figure 6. The measured velocities of the Hockley samples. (a) V_P and (b) V_S measured at different wave-propagation directions for salt-core sample H_1 . (c and d) V_S measurements, as the S-waves was polarized in the plane perpendicular to the wave-propagation direction for samples H_2 and H_3 .

To obtain velocity measurements from all three axial directions, we prepared sample H₂ with three mutually orthogonal pairs of parallel surfaces (Figure 5c). In each propagation direction, we made measurements as we rotated transducers to have S-wave polarized over 360° at 10° intervals. The 0°–180° polarization represents the vertical direction in situ. Compared with H₁, we found slightly higher values of V_P in all directions in H₂, as seen in Table 2. It is possible that the well-prepared measuring surfaces of H₂ reduced the contamination effects from the coring process. The V_S measure-

Table 2. Average velocities and densities of the Hockley salt samples: 0.5 MHz shear and 1 MHz compressional transducers were used. The root-mean-square (rms) deviation from the mean gives velocity variations as determined from the different wave-propagation directions for H₁ and various polarization directions for H₂ and H₃.

Samples	V _P (m/s)	V _S (m/s)	ρ (kg/m ³)
H ₁	Section a: 4555 ± 16	2697 ± 21	2180 ± 20
	Section b: 4552 ± 16	2696 ± 20	
	Section c: 4555 ± 1	2730 ± 22	
H ₂	X: 4597 ± 19	2686 ± 9	2200 ± 10
	Y: 4747 ± 12	2762 ± 30	
	Z: 4576 ± 15	2655 ± 14	
H ₃	X: 4345 ± 24	2580 ± 40	2150 ± 10
	Y: 4057 ± 38	2448 ± 34	
	Z: 4421 ± 19	2579 ± 27	

ments, as we rotated the shear-transducers, are plotted in Figure 6c. The data show slight S-wave splitting with propagation in the Y (horizontal core-axis in situ) direction. The fast V_S was found when the S-wave was polarized in a nearly transverse direction. Note also that the values of V_P and V_S in the Y-direction are somewhat higher,

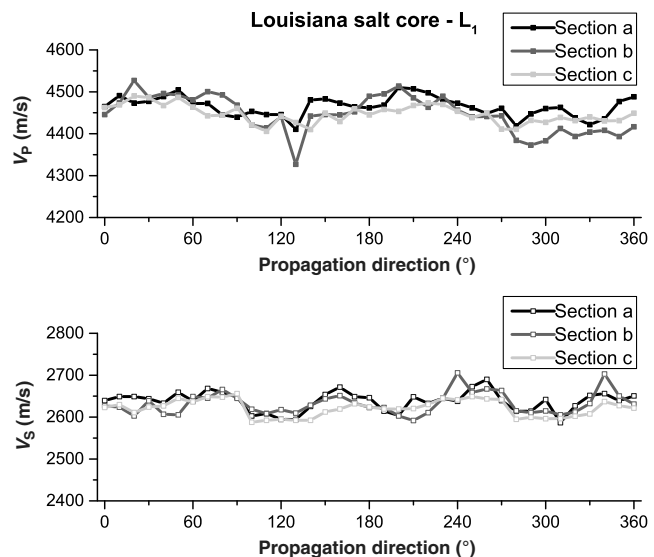


Figure 8. Velocity measurements on the Bayou Corne sample L₁ at room conditions. Velocities were plotted for S-wave propagation directions more than 360° at 10° intervals. The same measurements were taken in three equally spaced sections, 30 mm apart.

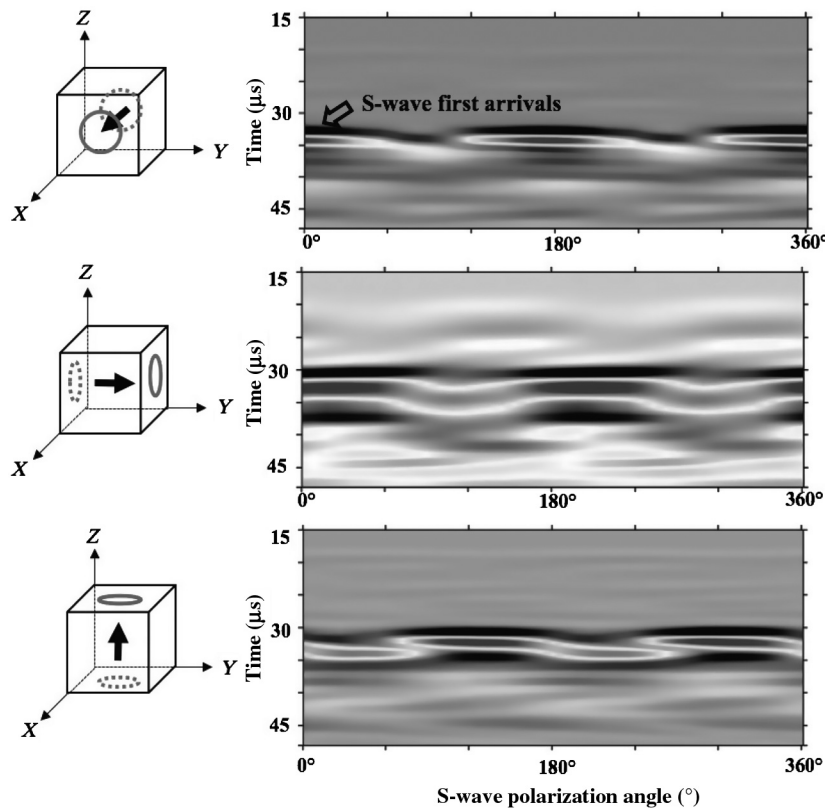


Figure 7. The S-wave first arrivals for the Hockley sample H₃. The left diagrams show the wave-propagation directions X, Y, and Z. The right plots show the recorded S-wave first arrivals for polarizations more than 360° at 10° intervals. Some S-wave splitting is observed.

approximately 4% for V_P , than in other directions of propagation. This variation may be associated with heterogeneity and tectonic stress effects, as well as disruption during drilling and excavation.

We measured H_3 in a similar manner to H_2 . The measurements in all three orthogonal directions of propagation indicated some S-wave splitting (seen in Figures 6d and 7). Inside the salt mine, especially where we obtained the samples, we observed vertically aligned fractures and cracks. The mining process (using explosive and mechanical means) might have changed the stress state of the salt dome. The stress redistribution can result in generation of zones with tensile stresses. Such stresses can easily initiate fractures because rock salt is weaker in tension than in compression (Silberschmidt and Silberschmidt, 2000). This may explain why V_P in the Z-axis (vertical) direction is higher than in the other two axial directions, whereas V_S recorded in the Y-direction showed S-wave splitting when the S-wave was polarized in the XZ-plane.

Measurements under confining pressure and at high temperature

We next investigated the effects of varying confining pressure and temperature on the elastic properties of the Bayou Corne salt-core samples. Three samples (L_1 , L_2 , and L_3) were prepared from a 101.6 mm (4 in) diameter salt core, sourced at a depth of 600 m in a vertical well. Halite amounted to approximately 97 wt%, with the remaining composition being mainly anhydrite.

We first measured L_1 in its cylindrical shape at room conditions using the same configuration as that for H_1 (Figure 5a). As shown in Figure 8, in three parallel sections, V_P and V_S showed slight variations when S-wave was polarized more than 360°. Such variations, approximately 3% for V_P and 4% for V_S , could be caused by the elongated crystals, microfractures, stress-release effects, or compositional variations. Velocities in the core axial direction, 4490 m/s

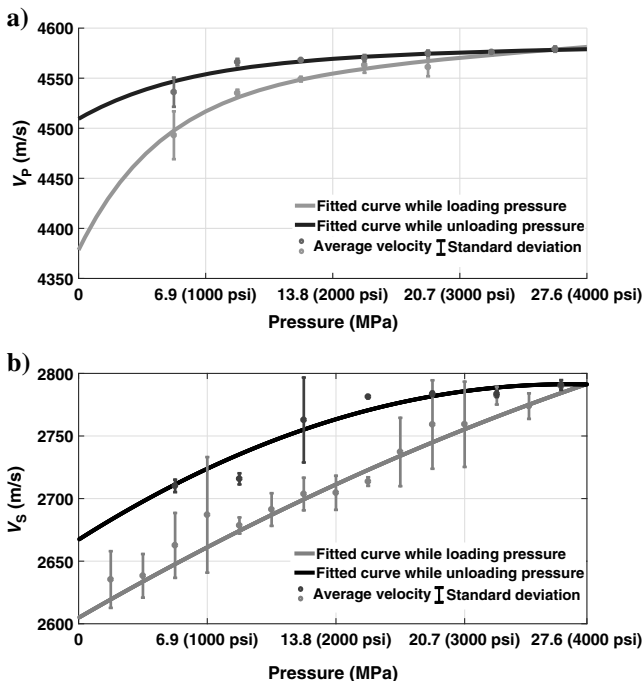


Figure 9. Velocity measurements on the Bayou Corne sample L_2 at varying pressures. (a) V_P and (b) V_S measured under triaxial pressure and at 25°C.

for V_P and 2620 m/s for V_S , are close to the average velocities over all directions. The measured density was $2150 \pm 1 \text{ kg/m}^3$ (Zong et al., 2015).

Stress effects.—The effects of stress were then studied for the 46 mm diameter salt plug L_2 . We measured the velocity in the core axial direction under triaxial pressure from 0 to 28 MPa (0–4000 psi) at 25°C. Figure 9 shows the least-squares best-fit curves for measured velocities during the loading (gray curves) and unloading process (black curves). As pressure rose, V_P and V_S increased from 4400 to 4800 m/s and 2500 to 2800 m/s. In the CT scanning images in Figure 10, the main gray mass is halite, whereas the white dots are heterogeneities with higher densities, such as anhydrite. We observed microcracks and fractures (black discontinuities) before loading as seen in Figure 10a. The high triaxial pressure closed these microcracks, and these microcracks remained largely closed after unloading (Figure 10b). The closure of microcracks may be the main cause of the rapid increase in velocity during the first 7 MPa (1000 psi) of pressure increase. The velocity curves flattened with further pressure increments. In unloading from 28 to 0 MPa, V_P and V_S dropped 70 and 120 m/s, respectively. The velocities did not return to their initial values after unloading, likely due to the cracks

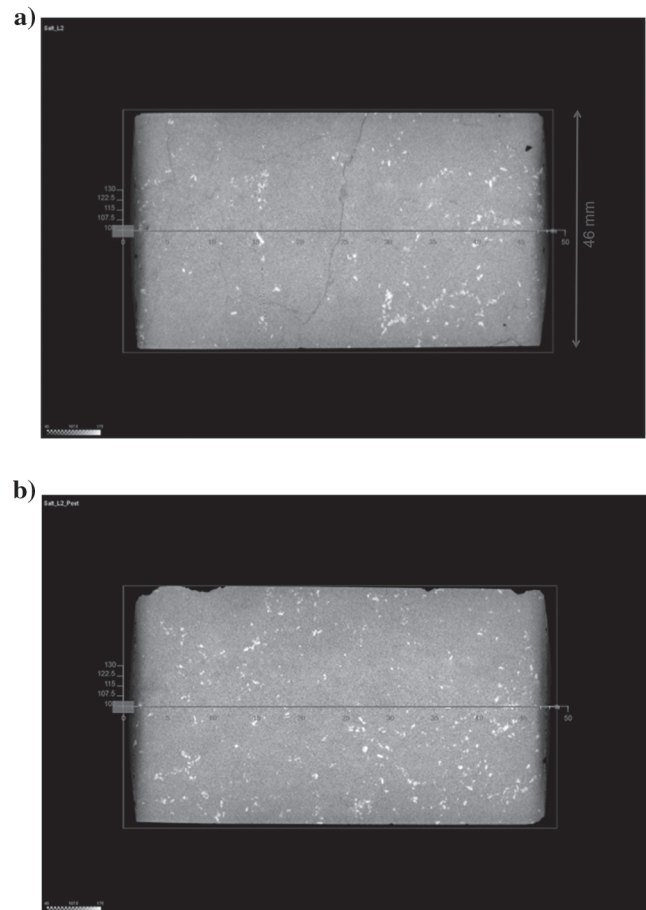


Figure 10. The CT scanning results for the Bayou Corne salt plug L_2 . (a) Microfractures and cracks are visible before the triaxial pressure test. (b) Most microfractures and cracks are closed after the triaxial pressure test. Note that the density distributions are somewhat different because the images were taken from different cross sections.

having healed. In that case, the increment of approximately 95 m/s for V_P and 64 m/s for V_S after cracks healing might provide some references for salt-core measurements before any damage recover processes.

Stress and temperature effects.—We further investigated the in situ elastic behavior of the 25 mm diameter Bayou Corne salt plug, L_3 , following specific confining pressure and temperature paths. The measurements were conducted by Core Laboratories in Houston. To avoid some of the effects of externally induced microcracks as identified in the stress-effect tests, we used values recorded during the processes of decreasing pressure and temperature. We found that increasing the pressure increased velocity, as it also has done in the previous tests on L_1 (seen in Figure 11). Increasing the temperature tended to decrease the velocity. Although the temperature and pressure generally increase deeper in the subsurface, they have opposite effects on salt velocities. It is consistent with some earlier results (e.g., Wang, 2001; King, 2005). With reference to Figure 11, the least-squares best-fit surfaces for observe velocities (in m/s) and

elastic moduli (in GPa) versus confining pressure, P (in MPa) [0–83 MPa (0–12,000 psi)] and temperature, T (in °C) [23°C–93°C (75°F–200°F)] are

$$V_P = 4608 + 1.801P - 1.532T + 3.476 \times 10^{-3}PT - 1.153 \times 10^{-2}P^2 - 5.122 \times 10^{-3}T^2, \quad (2)$$

$$V_S = 2662 + 0.9256P - 2.764T - 7.203 \times 10^{-4}PT - 3.825 \times 10^{-3}P^2 + 1.403 \times 10^{-2}T^2, \quad (3)$$

$$K = 25.49 + 2.155 \times 10^{-2}P + 2.76 \times 10^{-3}T + 6.46 \times 10^{-5}PT - 1.58 \times 10^{-4}P^2 - 2.23 \times 10^{-4}T^2, \quad (4)$$

$$G = 15.31 + 1.058 \times 10^{-2}P - 3.567 \times 10^{-2}T - 1.313 \times 10^{-5}PT - 4.339 \times 10^{-5}P^2 + 2.056 \times 10^{-4}T^2, \quad (5)$$

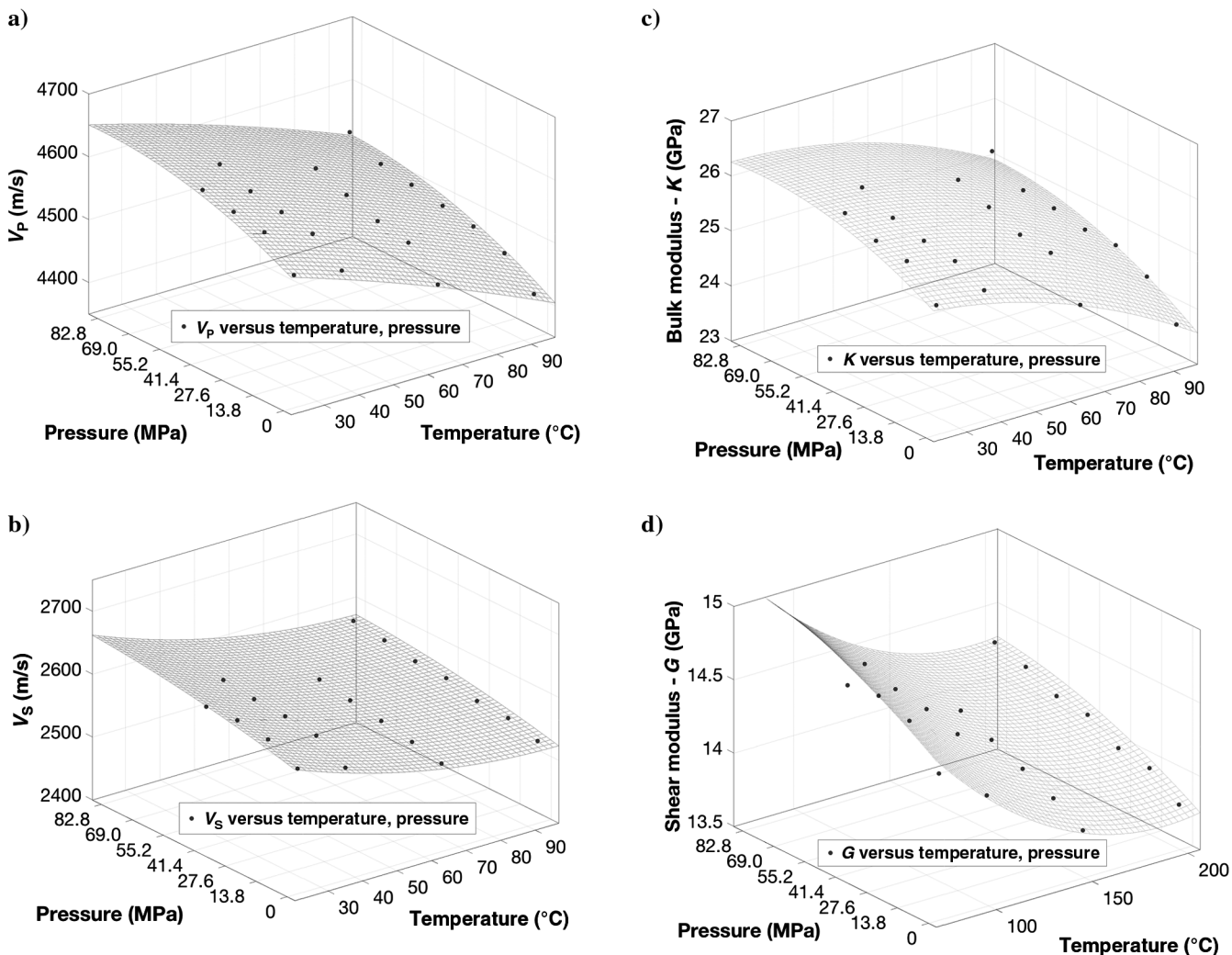


Figure 11 The least-squares best-fit surfaces for (a) V_P , (b) V_S , (c) K , bulk modulus, and (d) G , shear modulus versus confining pressure and temperature of Bayou Corne sample L_3 .

where K and G are the bulk and shear modulus, respectively. These best-fit equations within the measured pressure and temperature ranges give an $R^2 > 95\%$, and standard deviations of less than 10 m/s and 0.15 GPa for the velocities and elastic moduli.

Laminated salt samples from the Zipaquirá Salt Mine, Colombia

The allochthonous Zipaquirá salt deposits are located 50 km north of the margin of a high valley, the Sabana de Bogotá. They have undergone flowing, faulting, and deformation; also, they were documented to have large amounts of clay minerals, calcite, halite, magnesite, and pyrite in the argillaceous rock salt (McLaughlin and Herrera, 1970). The measured samples were characterized by laminations of relatively pure halite with argillaceous components. Figure 12a shows one of the tested samples Z_1 . The interbedded argillaceous halite layer was approximately 30 mm thick. Figure 12b shows an example of the laminations in the salt mine itself. Our XRD tests also had indicated a considerable amount of silicates and carbonates (shown in Figure 2).

To obtain the velocities for dirty and clean salts, we cut the sample into an argillaceous salt part (Z_{1a}) and a light-colored halite part (Z_{1b}) (Figure 12a). The parts Z_{1a} and Z_{1b} were measured using a pair of 1 MHz compressional transducers. The average velocities for the dark argillaceous salt were 3580 ± 480 m/s for V_p and 2100 ± 320 m/s for V_s . The light-colored halite part had an average V_p of 4290 ± 50 m/s and V_s of 2450 ± 20 m/s. The lower velocities found on the argillaceous salt are probably caused by the increasing amount of clay minerals.

Another five small halite samples (Z_2 to Z_6) from the Zipaquirá mine were also measured using the same compressional-transducer set. The samples had diameters of approximately 25 mm. The dark rock-salt samples were “tinted” by the clay minerals. Figure 12c shows the measured velocities and densities of these Zipaquirá samples. We repeated the measurements three times for each sample and included the standard deviations. Compared with the pure GOM salt samples, the Zipaquirá samples tended to have lower V_p and V_s

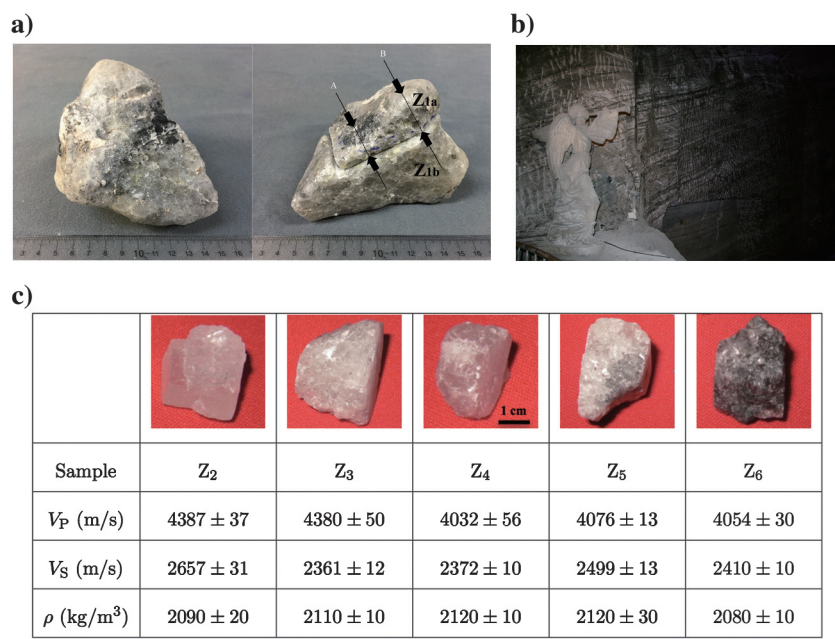
Figure. 12 Laminated salt in the Zipaquirá Salt Mine, Colombia. (a) The interbedded argillaceous halite layer in the tested sample, (b) photograph of the laminated salt formation inside the mine, (c) average velocities and densities measured from Zipaquirá rock salt samples Z_2 to Z_6 . The standard deviations give the accuracy of our measurements.

values. The velocity variations between different samples were much higher than those of the previous GOM samples. This is probably because of porosity and the inclusion of other lower velocity materials, such as clay. Such an observation is supported by the multiphase mixing law: effective elastic moduli of mixtures of halite with clay or anhydrite can be approximated theoretically by various bounds (the most often used are Hashin-Shtrikman and Voigt-Reuss bounds) (Mavko et al., 2009). As seen in Figure 13, the introduction of clay ($K = 27$ GPa, $G = 17$ GPa, and $\rho = 2680$ kg/m³) should decrease velocities, while increasing anhydrite content ($K = 66.5$ GPa, $G = 34$ GPa, and $\rho = 3000$ kg/m³) should increase velocities.

In some areas, thick intrasalt layers can be common and could introduce seismic reflections. For example, Strozyk et al. (2012) observe such reflections in the Netherlands from an offshore salt complex and suggest that further quantitative interpretations of the layering in the salt complex would be helpful for better seismic imaging. Landrø et al. (2011) identify an example of periodically stratified clay layers in a Cardona salt diapir in Spain and calculate a 5% velocity difference between the vertical and horizontal directions. Davison et al. (1996, 2012) interpret seismic data from Brazil’s Santos Basin to show strong reflections within the evaporite body due to interbedded impurities. Thus, we are reminded that heterogeneities in salt can substantially alter its seismic properties.

Crystalline salt samples from the Goderich Salt Mine, Ontario, Canada

Our samples G_1 and G_2 were taken from one of the world’s largest salt mines, the Goderich Salt Mine in Ontario, Canada, from a depth of approximately 525 m. This salt mine is located on the eastern edge of the stable Michigan Basin, where no major salt tectonism has occurred (Davis and Reynolds, 1996). Goderich salt is remarkably pure, is colorless to white, and it contains less than 2% impurities (Hewitt, 1962). Our mineralogy tests confirmed this, finding a composition of nearly 100% halite (NaCl). The samples had very clear cubic crystalline orientations similar to the “chevron-shaped” salt that is preserved worldwide (e.g., Permian San Andres



Formation of West Texas [Hovorka, 1987], western Canadian Devonian units [Sun, 1994], Lake Macleod, Western Australia [Warren, 2010]). We prepared two samples to obtain velocities in different directions (as shown in Figure 14): G_1 was prepared as a cube with X -, Y -, and Z -axes corresponding to the three orthogonal directions of cubic symmetry. G_2 was prepared with S-waves propagating in a direction 45° between the Y - and Z -axes. We used 0.5 MHz transducers for the Goderich samples velocity measurements. Figure 15 shows the recorded P- and S-wave first arrivals with respect to different S-wave polarization directions. The calculated values of velocity in each propagation direction and of density are given in Table 3. The velocity standard deviations give the variations from different S-wave polarization directions, whereas the density standard deviation came from three repeated measurements.

In the axial directions, V_P and V_S were constant at 4750 and 2465 m/s, respectively. There was no S-wave splitting observed for propagation along the principal axes (Figure 15a). We observed S-wave splitting for waves propagating in other, off-symmetry, directions. Figure 15b shows an example of wave propagation in a

direction at 45° to the Y - and Z -axes. The V_S variation was significant, approximately 18%; the fast V_S was 2920 m/s, whereas the slow V_S was 2465 m/s. V_P decreased to 4440 m/s in this direction, a 7.2% decrease compared with V_P in the three symmetric directions. The slight fluctuation of the S-wave first-arrival times for propagation along the Z -axis was likely caused by a small difference between the prepared Z -axis and the actual symmetry direction. Based on the assumption that the measured velocities are equal to the phase velocities in the directions of the three elastic axes of symmetry and at 45° between axes, the elastic constants for Goderich salt crystals were calculated as $C_{11} = 48.7$ GPa, $C_{44} = 13.1$ GPa, and $C_{12} = 11.9$ GPa (Zong, 2014).

Figure 16 shows the computed phase and group velocity distributions using the calculated elastic constants. V_P decreased when the P-waves propagated off of the three symmetry axes X , Y , and Z . Although V_{SV} increased when the SV-wave propagated in off-symmetry directions, V_{SH} was constant for propagation in the symmetry directions as well as within the symmetry planes XY , XZ , and YZ . V_{SH} increased when the SH-wave propagated out of the symmetry

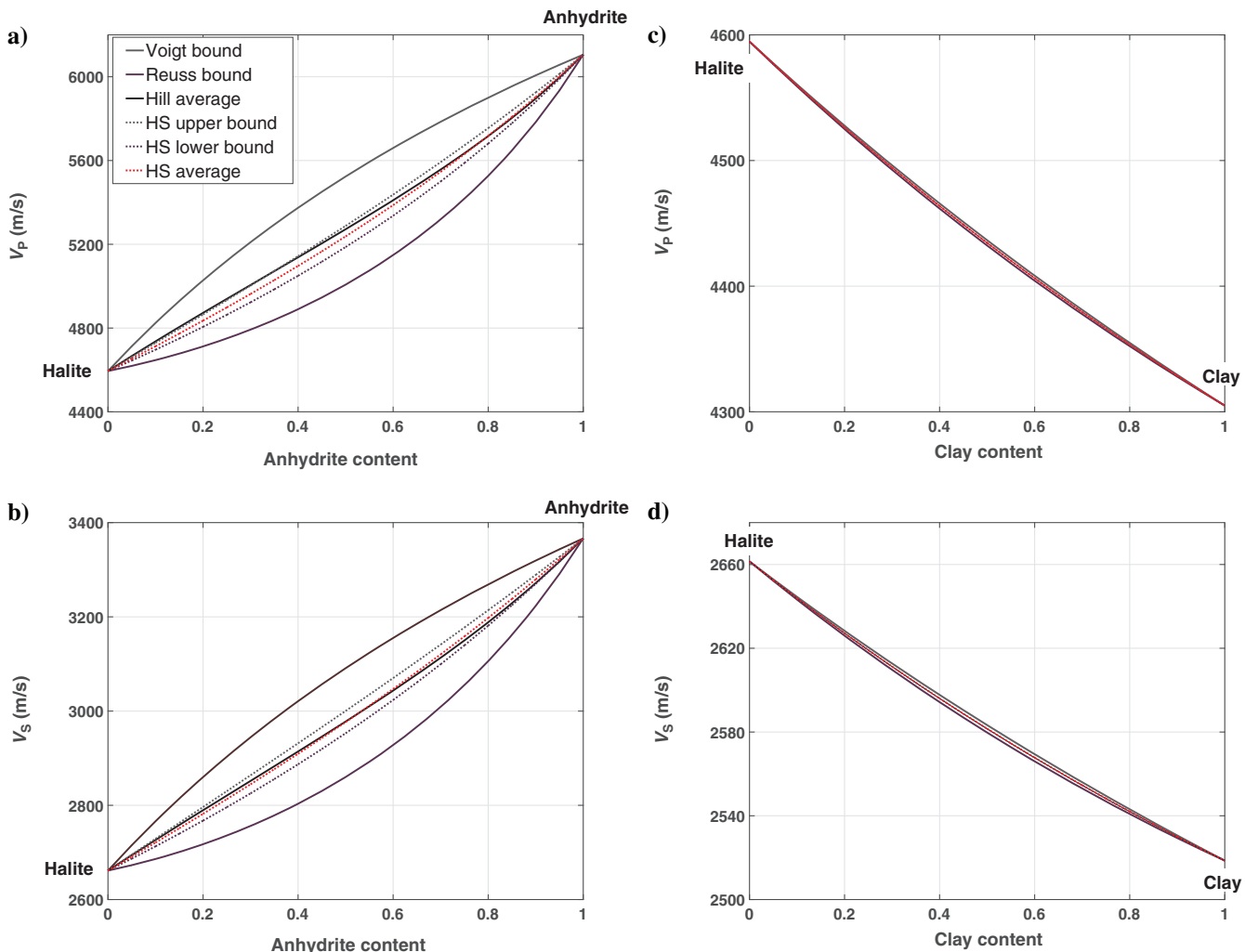


Figure 13. Examples of theoretical bounds and averages (Hashin-Shtrikman bounds and averages, as well as Voigt-Reuss bounds and Hill's averages) for mixing halite with anhydrite and clay. The (a) V_P and (b) V_S increase with the increasing anhydrite content in salt; (c) V_P and (d) V_S decrease with increasing clay content in salt. The elastic moduli used here were halite: $K = 25.2$ GPa, $G = 15.3$ GPa, $\rho = 2160$ kg/m 3 ; anhydrite: $K = 66.5$ GPa, $G = 34$ GPa, $\rho = 3000$ kg/m 3 ; and dry clay: $K = 27$ GPa, $G = 17$ GPa, $\rho = 2680$ kg/m 3 .

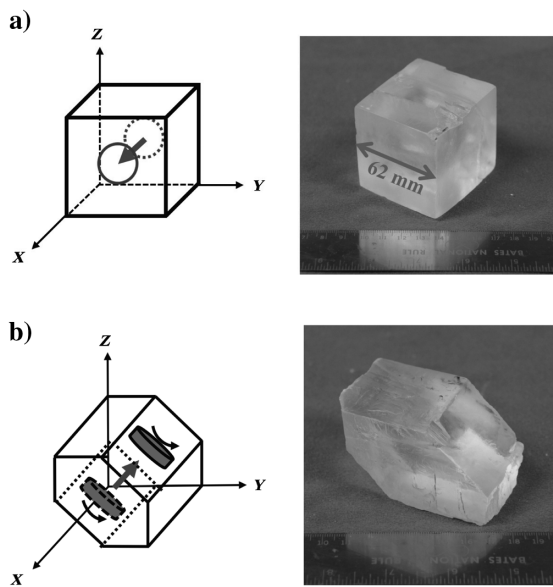
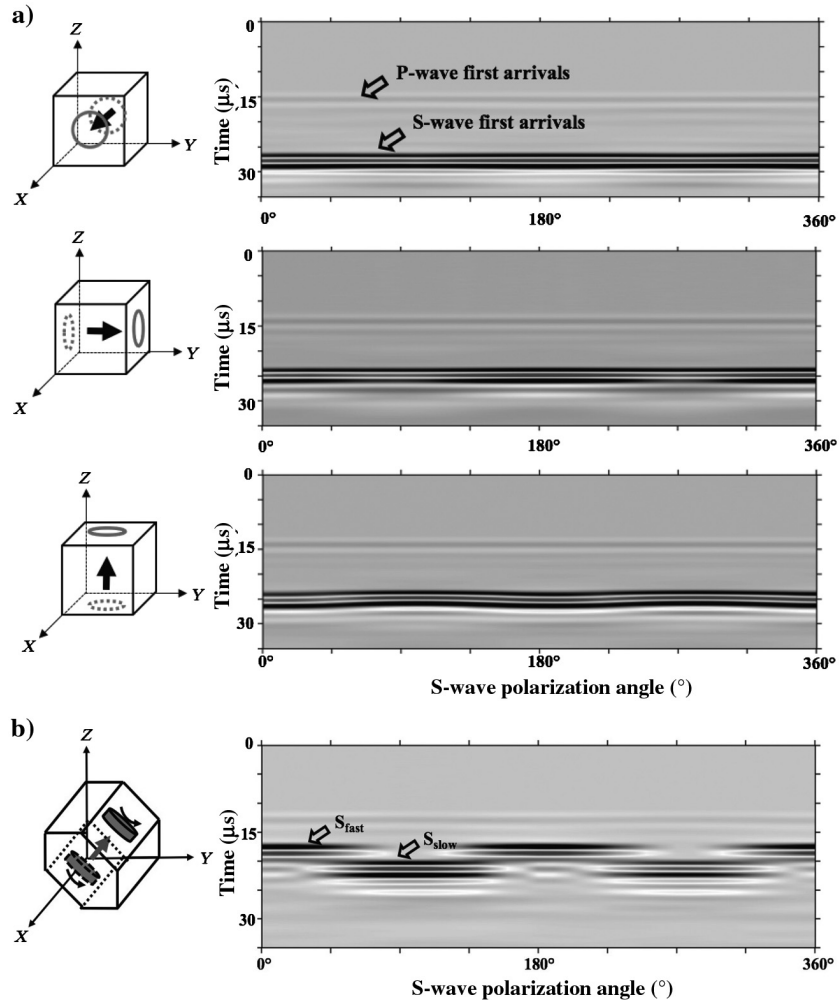


Figure 14. Wave-propagation directions in the Goderich salt-crystal samples G₁ and G₂. (a) Waves propagate along three axial symmetry directions X, Y, and Z, in the cubic sample G₁. (b) Waves propagate in the direction at 45° to X and Z in G₂.

Figure 15. The S-wave first arrivals of the Goderich salt samples at polarization direction from 0° to 360°. Left diagrams show the wave-propagation directions and the right plots show the arrivals. (a) S-wave arrivals in sample G₁. (b) S-wave splitting is apparent in sample G₂, for the propagation direction halfway between Y and Z.



planes. Within one symmetry plane, as an example shown in Figure 16g, the group and phase velocities are equal for P-, SV-, and SH-waves propagating in the three axial symmetry directions and at 45° between two axes. This justifies our assumption that the measured velocities in these directions are, in fact, the phase velocities.

To summarize, the allochthonous GOM and Zipaquirá salt may have experienced transportation, deformation, recrystallization, or interference with other components. We found that the GOM salt cores behaved largely isotropically, whereas the salt samples excavated from the mine displayed velocity anisotropy due to micro-cracks and fractures. The Zipaquirá samples showed transverse isotropy due to the heterogeneous thin layering in salt formations. The autochthonous Goderich salt preserved halite's crystalline structure and we observed cubic symmetry.

WELL LOGS IN THE GULF OF MEXICO

Most of the wells investigated here are located in the northern GOM area, and they are shown in Figure 17. We have also included three additional well-log suites, with V_S measurements from the Keathley Canyon. Salt deposits are typically identified in well logs by their nonradioactive, nonporous, low-density, high-velocity, electrically nonconductive, and soluble expressions (Tixier and Alger, 1970; LeFever and LeFever, 2005). Recognizing salt is usually

straightforward with these multiple log characteristics. Figure 18 shows the logs from one of the studied wells (latitude: 28.2814, longitude: -90.2052). In the following discussion, we excluded the heterogeneous parts from the well logs, and focused on the data extracted from pure rock salt. We averaged and plotted the log data at 30.48 m (100 ft) intervals.

Velocity versus depth

We plotted V_P (in m/s) versus vertical depth below the seafloor, D (in m), of the 142 northern GOM wells (Figure 17). We found a trend of velocity increasing with depth (Figure 19). We determine a least-squares linear best-fit to all of the data:

$$V_P = 4455 + 0.00478D. \quad (6)$$

The standard deviation of the fit is 100 m/s, which may be helpful as a general reference for velocity variations in the northern GOM area.

These variations may be due to small amounts of impurities or moisture, overburden pressure variations, or other ambient differences. For example, the water-depth differences (up to 2 km) in our study region could result in overburden pressure variations up to 20 MPa, using 0.44 psi/ft for the hydrostatic gradient in the GOM (Wallace et al., 1979; Warren, 2010).

The S-wave logs in the GOM are rare and perhaps are not as reliable as regular P-wave sonic logs. Nonetheless, we have included

Table 3. Measured velocities in different wave-propagation directions and density for the Goderich samples. The rms deviations from the mean give velocity variations as determined from different polarization directions.

Wave-propagation direction	V_P (m/s)	V_S (m/s)	ρ (kg/m^3)
X	4766 ± 4	2464 ± 2	2150 ± 10
Y	4761 ± 14	2468 ± 8	
Z	4756 ± 7	2463 ± 7	
Halfway between X and Y	4438 ± 11	$S_1: 2916 \pm 2, S_2: 2468 \pm 1$	

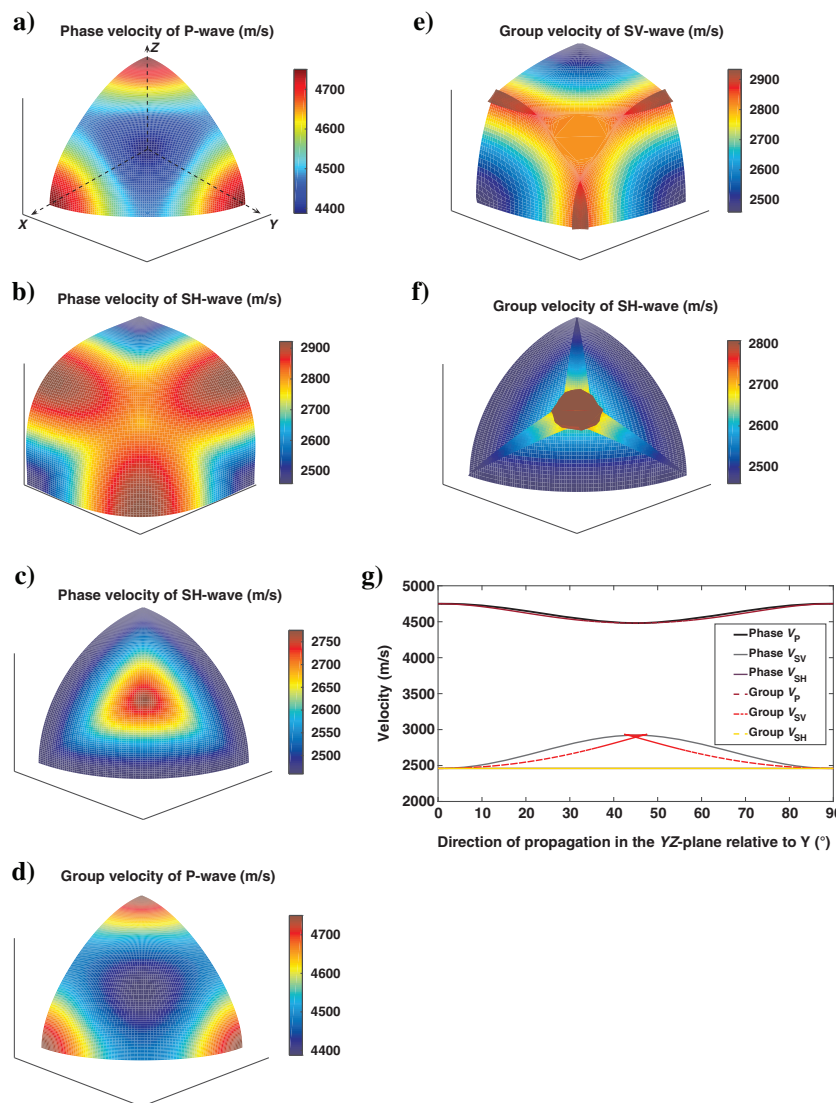


Figure 16. Phase velocity (a) V_P , (b) V_{SV} , (c) V_{SH} ; and group velocity (d) V_P , (e) V_{SV} , (f) V_{SH} distributions calculated in a cubic medium. The axes of cubic symmetry are indicated in panel (a). (g) The velocity distributions in a symmetry plane YZ . The velocities are calculated using the stiffness tensor of the Goderich salt samples $C_{11} = 48.7$ GPa, $C_{44} = 13.1$ GPa, and $C_{12} = 11.9$ GPa.

three wells with S-wave logs from the Keathley Canyon, as shown in Figure 17. The V_P and V_S curves from those three wells are plotted in Figure 20. We notice that for the Keathley Canyon, the V_P curves fit tightly to our previously determined $V_P(D)$ line. V_S ranged from 2280 to 2590 m/s. We further compared these sonic log values with the previous benchtop ultrasonic velocity measurements (shown as the gray range bars marked in the vertical axes in Figure 17) for salt cores in the GOM. It is noticeable that the sonic velocities are somewhat lower than the ultrasonic velocity measurements. Possibilities for such a difference include velocity dispersion, temperature, and pressure effects. As for velocity dispersion, Stewart et al. (1984) provide an equation to relate velocities at different frequencies, given an attenuation factor, as

Figure 17. Map of the northern GOM with locations for the 145 well-log suites used in this study. The 142 wells (yellow markers) from the northern GOM were provided by F. Hilterman and Geokinetics Inc., Houston. Three well-log suites in the Keathley Canyon were provided courtesy of S. Cornelius.

$$\frac{C(\omega_1)}{C(\omega_2)} = 1 + \frac{1}{\pi \cdot Q} \cdot \ln \frac{\omega_1}{\omega_2}, \quad (7)$$

where $C(\omega_1)$ and $C(\omega_2)$ are the phase velocities at frequencies ω_1 and ω_2 . Sears and Bonner (1981), using ultrasonic (1 MHz) measurements on a GOM salt core, find a $Q_P = 46$. Assuming a sonic-log frequency of 10 kHz, V_P from well logs in this attenuative salt could be approximately 3% lower than the ultrasonic measurements. This is approximately what we observed in our laboratory and in log averages.

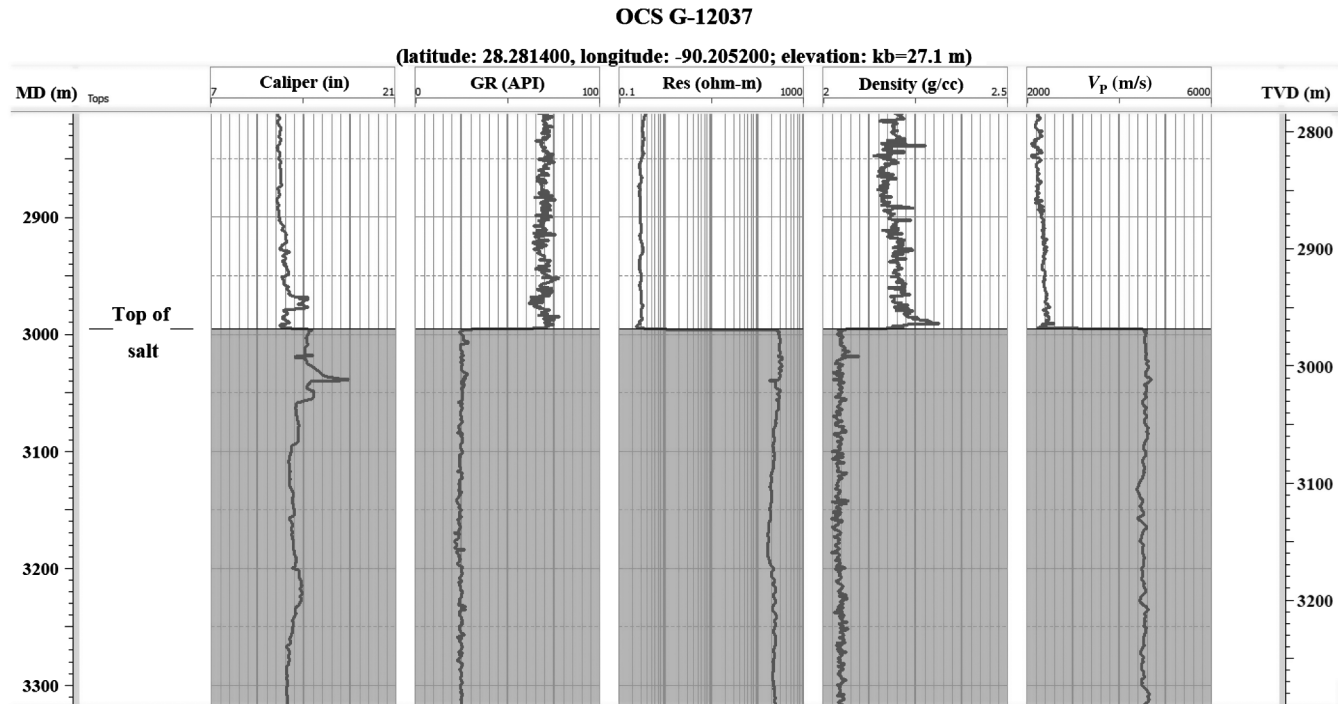
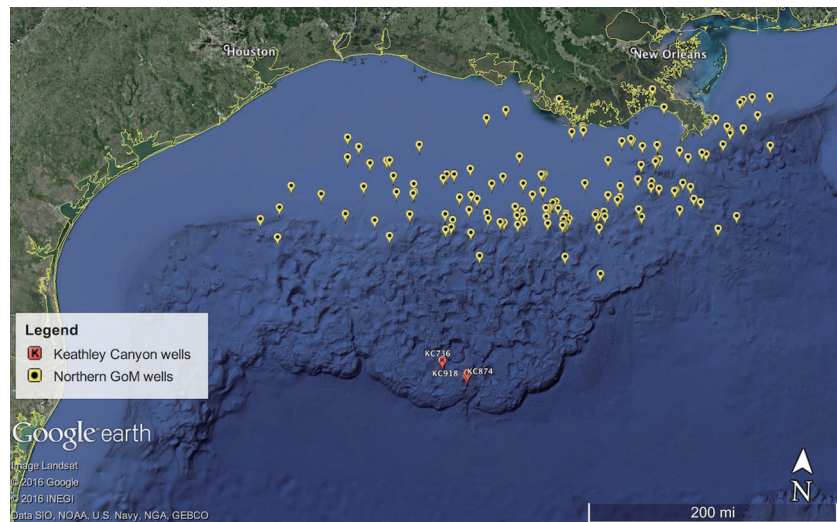


Figure 18. Example logs from a borehole drilled through a GOM salt formation. Log readings in the salt formation are highlighted in gray.

Velocity versus density

The electron density reading ρ_e from a conventional density well-logging tool can be corrected to formation bulk density ρ_b using $\rho_b = (A/2Z) \cdot \rho_e$, where A is the molecular weight of the compound and Z is the atomic number (Gluyas and Swarbrick, 2013). For halite ($A = 58.44$ and $Z = 28$), this equation can be written as

$$\rho_b = 1.044\rho_e. \quad (8)$$

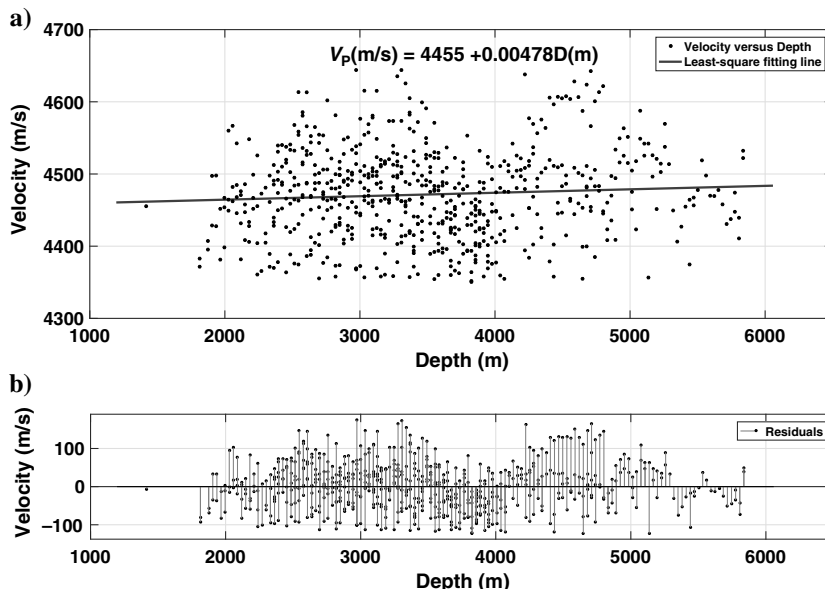


Figure 19. The V_p from 142 wells in the northern GOM region. (a) Velocity versus depth (below seafloor) from the logs. The straight line is the least-squares best fit: $V_p(\text{m/s}) = 4455 + 0.00478D(\text{m})$. (b) Residuals from the fitted line with a standard deviation of 100 m/s.

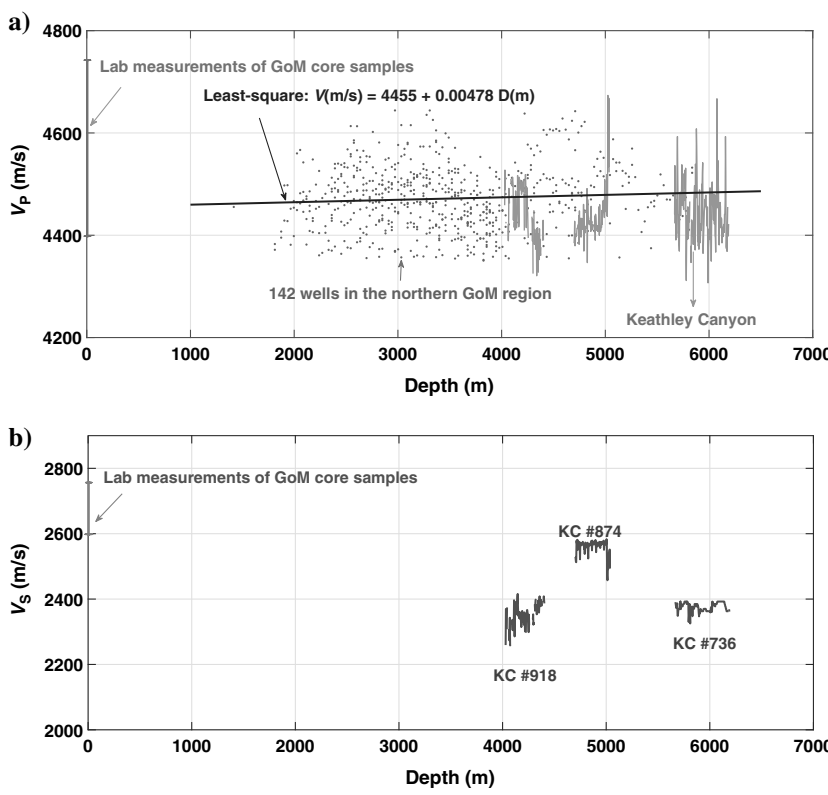


Figure 20. (a) The V_p from 142 northern Gulf wells logs and (a) V_p and (b) V_s from three Keathley Canyon well-log suites. The benchtop laboratory measurements for the GOM salt cores are plotted using the gray range marks at depth zero for comparison.

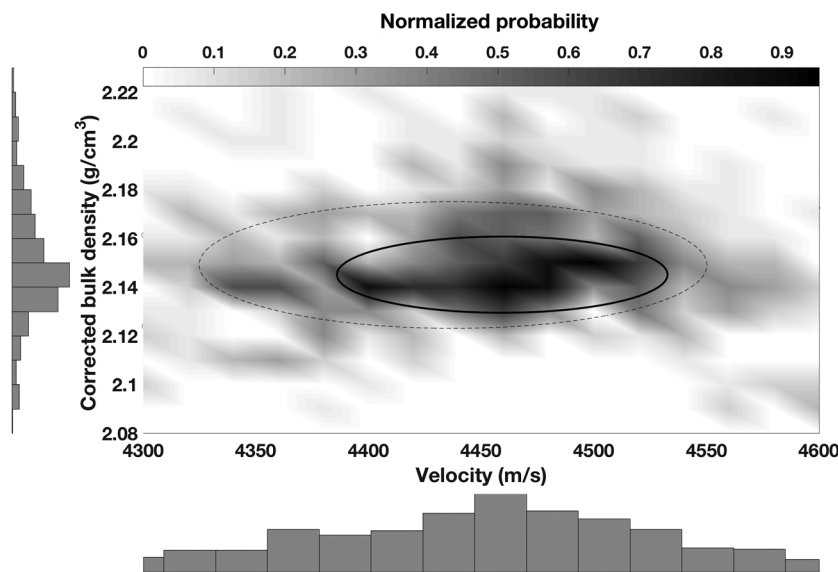


Figure 21. Crossplot of the corrected bulk density versus velocity for salt intervals from the log suites. The data distribution is colored according to the probability. The solid ellipse endorses the range of high probability. Data points outside the dashed ellipse are of low probability. The velocity and density histograms are plotted to show the distributions.

anhydrite: $V_P = 6500 \text{ m/s}$, $\rho = 2970 \text{ kg/m}^3$; and sylvite: $V_P = 3500 \text{ m/s}$, $\rho = 1900 \text{ kg/m}^3$ (Jones and Davison, 2014).

CONCLUSION

We studied the effects of composition, crystalline structure, pressure, and temperature on the elastic properties of rock salt. Salt cores from the Hockley Salt Dome and the Bayou Corne Salt Dome in the GOM appear generally isotropic. The Hockley salt block displayed some anisotropic character possibly due to the effects of excavation. The Zipaquirá salt samples showed that laminations introduced anisotropy when the alternating layers displayed different elastic properties. Velocities measured in this argillaceous salt were somewhat lower than in pure halite. We observed cubic anisotropy in the Goderich halite crystals. The calculated elastic constants of cubic symmetry are $C_{11} = 48.7 \text{ GPa}$, $C_{44} = 13.1 \text{ GPa}$, and $C_{12} = 11.9 \text{ GPa}$. Traveltime differences caused by such cubic anisotropy could be substantial. We observed that increasing confining pressure increased V_P and V_S , whereas increasing temperature decreased V_P and V_S . The best-fit equations may be helpful to estimate formation velocities at a given temperature and pressure.

Well-log analysis provided *in situ* values in the GOM area. An empirical relationship for V_P versus depth below seafloor was given from 142 well-log suites in the northern GOM, where $V_P(\text{m/s}) = 4455 + 0.00478D(\text{m})$, with a standard deviation of 100 m/s. Our sonic-log V_P data from the Keathley Canyon fit our previously established line fairly closely, while our S-wave log data ranges from 2280 to 2590 m/s for V_S . The log values were slightly lower than the ultrasonic measurements of V_P and V_S . One possibility to explain this difference could be velocity dispersion associated with attenuation. For example, a $Q_P = 46$ would result in a V_P difference of 3%. The corrected bulk density of rock salt clusters approximately 2160 kg/m^3 , with a variation of $\pm 30 \text{ kg/m}^3$. The well-log values, with multiple influencing factors and variations, should be helpful

in building velocity models, generating synthetic seismograms, and understanding salt properties generally.

ACKNOWLEDGMENTS

This work is supported by the Allied Geophysical Laboratories at the University of Houston. We gratefully appreciate F. Hilterman, Geokinetics Inc., Houston, and S. Cornelius for the use of their well-log data. We thank J. Warneke, Texas Brine Corporation, and M. Serna, for donating the salt samples. We also thank D. Jiao, E. Krauss, and C. Whitney, Core Laboratories Inc., for carrying out the ultrasonic measurements at varying confining pressures and temperatures. We thank J. Korp, Y. Gao, and W. Yang at the University of Houston for their assistance with the XRD and ICP-MS tests. Thanks to L. Thomsen, S. Leaney, L. Huang, D. Coleff, A. Bilal, and Y. Gan for helpful discussions. We wish to express our deep appreciation to J. Brown of the University of Stavanger for his petrophysical insights and detailed review of this work. In addition, we thank all the editors and anonymous reviewers for their constructive reviews of the paper.

REFERENCES

- Anderson, R. E., D. H. Eargle, and B. O. Davis, 1973, Geologic and hydrologic summary of salt domes in Gulf Coast region of Texas, Louisiana, Mississippi, and Alabama: U.S. Geological Survey Open-File Report, 4339-2.
- Brown, R. J., and Z. Sun, 1993, An underground seismic-anisotropy experiment in a salt mine: CREWES Research Report, University of Calgary, 1–11.
- Davis, G. H., and S. Reynolds, 1996, Structural geology of rocks and regions, 2nd ed.: Wiley.
- Davison, I., I. Alsop, and D. Blundell, 1996, Salt tectonics: Some aspects of deformation mechanics: Geological Society of London, Special Publications, 1–10.
- Davison, I., L. Anderson, and P. Nuttall, 2012, Salt deposition, loading and gravity drainage in the Campos and Santos salt basins: Geological Society of London, Special Publications, 159–174.
- Gevantman, L. H., J. Lorenz, J. Haas, Jr., M. Clyne, and R. Potter, 1981, Physical properties data for rock salt: U.S. Department of Commerce, National Bureau of Standards Monograph, 214.
- Glynn, J., and R. Swarbrick, 2013, Petroleum geosciences: John Wiley & Sons.
- Hewitt, D. F., 1962, Salt in Ontario: Industrial Mineral Report, Ontario Department of Mines, 38.
- Hovorka, S., 1987, Depositional environments of marine-dominated bedded halite, Permian San Andres Formation, Texas: Sedimentology, **34**, 1029–1054, doi: [10.1111/j.1365-3091.1987.tb00591.x](https://doi.org/10.1111/j.1365-3091.1987.tb00591.x).
- Hudec, M. R., and M. P. Jackson, 2007, Terra infirma: Understanding salt tectonics: Earth-Science Reviews, **82**, 1–28, doi: [10.1016/j.earscirev.2007.01.001](https://doi.org/10.1016/j.earscirev.2007.01.001).
- Jackson, M. P., 1984, Atlas of salt domes in the East Texas basin: University of Texas, Bureau of Economic Geology.
- Jackson, M. P. A., D. G. Roberts, and S. Nelson, 2008, Salt tectonics: A global perspective: AAPG.
- Ji, S., T. Huang, K. Fu, and Z. Li, 2011, Dirty salt velocity inversion: The road to a clearer subsalt image: Geophysics, **76**, no. 5, WB169–WB174, doi: [10.1190/1.3513718](https://doi.org/10.1190/1.3513718).
- Jones, I. F., and I. Davison, 2014, Seismic imaging in and around salt bodies: Interpretation, **2**, no. 4, SL1–SL20, doi: [10.1190/INT-2014-0033.1](https://doi.org/10.1190/INT-2014-0033.1).
- King, M. S., 2005, Rock-physics developments in seismic exploration: A personal 50-year perspective: Geophysics, **70**, no. 6, 3ND–8ND, doi: [10.1190/1.2107947](https://doi.org/10.1190/1.2107947).
- Landrø, M., C. Puigdefabregas, and B. Arntsen, 2011, Anisotropy in the salt outcrop at Cardona, Catalonia: Implications for seismic imaging: First Break, **29**, 41–45.

- Leaney, W. S., B. E. Hornby, A. J. Campbell, S. Viceer, M. Albertin, and A. Malinverno, 2004, Sub-salt velocity prediction with a look-ahead AVO walkaway: 74th Annual International Meeting, SEG, Expanded Abstracts, 2474–2476.
- LeFever, J. A., and R. D. LeFever, 2005, Salts in the Williston Basin, North Dakota: North Dakota Geological Survey.
- Leslie, A. B., G. M. Harwood, and A. C. Kendall, 1997, Geochemical variations within a laminated evaporite deposit: Evidence for brine composition during formation of the Permian Castile Formation, Texas and New Mexico, USA: *Sedimentary Geology*, **110**, 223–235, doi: [10.1016/S0037-0738\(96\)00087-5](https://doi.org/10.1016/S0037-0738(96)00087-5).
- Leveille, J. P., I. F. Jones, Z.-Z. Zhou, B. Wang, and F. Liu, 2011, Subsalt imaging for exploration, production, and development: A review: *Geophysics*, **76**, no. 5, WB3–WB20, doi: [10.1190/geo2011-0156.1](https://doi.org/10.1190/geo2011-0156.1).
- Mavko, G., T. Mukerji, and J. Dvorkin, 2009, *The rock physics handbook: Tools for seismic analysis of porous media*: Cambridge University Press.
- Mavko, G., and R. Nolen-Hoeksema, 1994, Estimating seismic velocities at ultrasonic frequencies in partially saturated rocks: *Geophysics*, **59**, 252–258, doi: [10.1190/1.1443587](https://doi.org/10.1190/1.1443587).
- McLaughlin, D. H., Jr., and M. A. Herrera, 1970, Economic geology of the Zipaquirá quadrangle and adjoining area, Department of Cundinamarca, Colombia: U.S. Geological Survey Open-File Report, 141.
- Pratten, N., 1981, The precise measurement of the density of small samples: *Journal of Materials Science*, **16**, 1737–1747, doi: [10.1007/BF00540619](https://doi.org/10.1007/BF00540619).
- Raup, O. B., 1970, Brine mixing: An additional mechanism for formation of basin evaporates: *AAPG Bulletin*, **54**, 2246–2259.
- Raymer, D. G., J. M. Kendall, D. Pedlar, R. R. Kendall, M. C. Mueller, and G. J. Beaudoin, 2000a, The significance of salt anisotropy in seismic imaging: 70th Annual International Meeting, SEG, Expanded Abstracts, 562–565.
- Raymer, D. G., A. Tommasi, and J. M. Kendall, 2000b, Predicting the seismic implications of salt anisotropy using numerical simulations of halite deformation: *Geophysics*, **65**, 1272–1280, doi: [10.1190/1.1444818](https://doi.org/10.1190/1.1444818).
- Sears, F. M., and B. P. Bonner, 1981, Ultrasonic attenuation measurement by spectral ratios utilizing signal processing techniques: *IEEE Transactions on Geoscience and Remote Sensing*, **GE-19**, 95–99, doi: [10.1109/TGRS.1981.350359](https://doi.org/10.1109/TGRS.1981.350359).
- Silberschmidt, V., and V. Silberschmidt, 2000, Analysis of cracking in rock salt: *Rock Mechanics and Rock Engineering*, **33**, 53–70, doi: [10.1007/s006030050004](https://doi.org/10.1007/s006030050004).
- Stewart, R. R., N. Dyaar, B. Omoboya, J. De Figueiredo, M. Willis, and S. Sil, 2012, Physical modeling of anisotropic domains: Ultrasonic imaging of laser-etched fractures in glass: *Geophysics*, **78**, no. 1, D11–D19, doi: [10.1190/geo2012-0075.1](https://doi.org/10.1190/geo2012-0075.1).
- Stewart, R. R., P. D. Huddleston, and T. K. Kan, 1984, Seismic versus sonic velocities: A vertical seismic profiling study: *Geophysics*, **49**, 1153–1168, doi: [10.1190/1.1441745](https://doi.org/10.1190/1.1441745).
- Strozyk, F., H. Van Gent, J. Urai, and P. A. Kukla, 2012, 3D seismic study of complex intra-salt deformation: An example from the Upper Permian Zechstein 3 stringer, western Dutch offshore: *Geological Society of London, Special Publications*, 489–501.
- Sun, Z., 1994, Seismic anisotropy in salt from theoretical study, modelling and field experiments: M.S. thesis, University of Calgary.
- Tixier, M., and R. Alger, 1970, Log evaluation of nonmetallic mineral deposits: *Geophysics*, **35**, 124–142, doi: [10.1190/1.1440070](https://doi.org/10.1190/1.1440070).
- Vernik, L., and X. Liu, 1997, Velocity anisotropy in shales: A petrophysical study: *Geophysics*, **62**, 521–532, doi: [10.1190/1.1444162](https://doi.org/10.1190/1.1444162).
- Wallace, R., T. Kraemer, R. Taylor, and J. Wesselman, 1979, Assessment of geopressured-geothermal resources in the northern Gulf of Mexico basin: U.S. Geological Survey Circular 790, 132–155.
- Wang, Z., 2001, Fundamentals of seismic rock physics: *Geophysics*, **66**, 398–412, doi: [10.1190/1.1444931](https://doi.org/10.1190/1.1444931).
- Warren, J. K., 2010, Evaporites through time: Tectonic, climatic and eustatic controls in marine and nonmarine deposits: *Earth-Science Reviews*, **98**, 217–268, doi: [10.1016/j.earscirev.2009.11.004](https://doi.org/10.1016/j.earscirev.2009.11.004).
- Willis, M. E., R. Lu, X. Campman, M. Nafi Toksöz, Y. Zhang, and M. V. de Hoop, 2006, A novel application of time-reversed acoustics: Salt-dome flank imaging using walkaway VSP surveys: *Geophysics*, **71**, no. 2, A7–A11, doi: [10.1190/1.2187711](https://doi.org/10.1190/1.2187711).
- Zong, J., 2014, Elastic properties of salt: Laboratory measurements, well-log analysis, and a seismic survey over the Hockley Salt Mine, Texas: M.S. thesis, University of Houston.
- Zong, J., R. R. Stewart, N. Dyaar, and M. Myers, 2015, Elastic properties of rock salt: Lab measurements and well log analysis in the Gulf of Mexico: 85th Annual International Meeting, SEG, Expanded Abstracts, 3095–3099.